

Multi-scale Latent Point Consistency Models for 3D Shape Generation

Bi'an Du, *Student Member, IEEE*, Wei Hu, *Senior Member, IEEE*, and Renjie Liao

Abstract—Consistency Models (CMs) have significantly accelerated the sampling process in diffusion models, yielding impressive results in synthesizing high-resolution images. To explore and extend these advancements to point-cloud-based 3D shape generation, we propose a novel Multi-scale Latent Point Consistency Model (MLPCM). Our MLPCM follows a latent diffusion framework and introduces a hierarchy of latent representations, ranging from point-level to super-point levels, each corresponding to a different spatial resolution. We design a multi-scale latent integration module along with 3D spatial attention to effectively denoise the point-level latent representations conditioned on those from multiple super-point levels. Additionally, we propose a latent consistency model, learned through consistency distillation, that compresses the prior into a one-step generator. This significantly improves sampling efficiency while preserving the performance of the original teacher model. Extensive experiments on standard benchmarks ShapeNet and ShapeNet-Vol demonstrate that MLPCM achieves a 100× speedup in the generation process, while surpassing state-of-the-art diffusion models in terms of both shape quality and diversity.

Index Terms—Hierarchical latent space, 3D spacial attention, 3D point cloud generation, consistency models.

I. INTRODUCTION

Generative 3D shape modeling is fundamental to many 3D vision and graphics applications, enabling digital artists to produce realistic and high-quality assets [1, 2, 3, 4, 5, 6]. For these models to be practically effective, they must provide flexibility for interactive refinement, support the synthesis of diverse shape variations, and generate smooth meshes that seamlessly integrate into standard graphics pipelines.

Driven by rapid progress in text, images, and video generation models, 3D shape generation has likewise advanced progress. Techniques based on variational autoencoders (VAEs) [7, 8], generative adversarial networks (GANs) [9, 10, 11], and normalizing flow models [12, 13] have been proposed to generate 3D shapes. Recently, diffusion-based models [14] and their latent diffusion variants [2, 15] have achieved state-of-the-art results in this domain.

Despite notable progress, substantial obstacles remain when applying diffusion models to 3D shapes that are represented as point clouds. Point sets are unordered, irregular, and often highly non-uniform in density, which complicates both neighborhood construction and feature aggregation [16, 17, 18]. A single radius may fail to capture thin structures while a large radius may blur sharp edges, and k-nearest-neighbor graphs

can become unstable under varying sampling density [17, 19]. Real data frequently contain noise, outliers, holes, and partial coverage from limited viewpoints [20, 21], so the denoiser must be robust to missing regions while still reconstructing fine details. In addition, 3D geometry introduces invariances and symmetries that are easy to violate. Models that are not carefully designed with respect to translation, rotation, and scale may overfit to coordinate frames or camera poses [22, 23]. These factors push the denoising network to learn representations that respect both local geometric primitives such as edges, corners, and small parts, and global object level regularities such as symmetry, topology, and part arrangement. Capturing these patterns jointly is essential for producing high quality point sets that are faithful at a small scale while remaining structurally coherent at a large scale.

A promising strategy is to diffuse in a learned latent space where shapes are summarized into compact codes that suppress nuisance variation and concentrate information about structure [2, 24]. Learning in latent space reduces computational cost and can improve stability, yet relying on a single level of latent representation has proved insufficient. A single scale cannot simultaneously preserve tiny geometric details and encode global layout, which leads to oversmoothed reconstructions or broken long range dependencies [25]. Effective 3D generation therefore requires multiple levels or resolutions together with mechanisms that let information flow across them so that coarse latents guide overall structure while finer latents supply detail where needed [2]. A second challenge concerns practicality. The sampling process in diffusion models typically requires many iterative evaluations of the denoiser, which results in slow generation and high memory consumption [26]. Classifier free guidance and other conditioning signals further increase the computational burden [27]. Without acceleration, these costs hinder real world use in interactive modeling, editing, completion from sparse inputs, or deployment within larger 3D pipelines [28, 29]. Reducing the number of steps while preserving quality, for example through consistency distillation or higher order solvers in latent space [30, 31], remains critical for making diffusion-based point cloud generators both accurate and efficient.

Here we introduce Multi-scale Latent Point Consistency Models (MLPCM), a generative model for 3D shape synthesis that follows the latent diffusion paradigm while addressing the joint learning of fine local geometry and long range structural coherence within a single framework. The architecture is a hierarchical variational autoencoder that encodes each shape into multiple levels of latent variables, from point level to super-point levels, each aligned with a specific spatial resolution. These latents form an explicit hierarchy

B. Du and W. Hu are with Wangxuan Institute of Computer Technology, Peking University, No. 128 Zhongguancun North Street, Beijing, China. E-mail: pkudba@stu.pku.edu.cn, forhuwei@pku.edu.cn

R. Liao is with Department of Electrical and Computer Engineering, University of British Columbia, Vancouver, Canada. E-mail: rjliao@ece.ubc.ca
Corresponding author: Wei Hu.

in the encoder so that information flows in both top down and bottom up directions. Coarse semantic latents provide guidance for the organization of global structure, while fine latents inject detail that refines and corrects coarse hypotheses. Diffusion operates on point level latents, which concentrates stochasticity where geometric detail resides and keeps higher level latents clean and semantically stable. A multi-scale latent integration module then conditions the denoiser by modulating noisy point latents with super-point latents from several scales. This cross-scale conditioning encourages the emergence of compositional regularities, supports reuse of part-level patterns across categories, and improves data efficiency under sparse or partial observations.

To further strengthen geometric fidelity and controllability, the denoising network integrates a 3D spatial attention mechanism whose bias term derives from pairwise Euclidean distances. This bias respects rigid transformations and encourages attention to concentrate on geometrically proximate regions while preserving the capacity to aggregate information across the entire shape when long range dependencies are beneficial. Training optimizes a hierarchical evidence lower bound for the VAE together with the standard latent diffusion objective. After training, consistency distillation in latent space yields a latent consistency model that preserves the visual quality of the diffusion sampler while reducing the number of refinement steps, which enables rapid sampling for interactive editing and conditional generation. In combination, hierarchical latent organization, multi-scale integration, geometry aware attention, and accelerated inference provide a practical foundation for downstream tasks such as completion from sparse views, structure-preserving editing, controllable synthesis with part level constraints, and conditional reconstruction from partial point clouds, while also improving robustness to noise, distribution shift, and limited supervision.

In summary, our main contributions are as follows:

- We propose a novel Multi-scale Latent Point Consistency Model for 3D shape generation, which builds a diffusion model with a hierarchical latent space, leveraging representations ranging from point to super-point levels.
- We propose a multi-scale latent integration module along with a 3D spatial attention mechanism to enable the denoiser to focus on salient neighbourhoods while maintaining global consistency, resulting in sharper topology and more uniform point distribution.
- We extend consistency distillation to unstructured point-latent spaces and couple it with multi-scale latent integration, yielding a student that inherits multi-scale semantics and generates 3D shapes in one to four steps without loss of visual or structural fidelity.
- Experiments demonstrate that our method outperforms existing approaches on the widely used ShapeNet benchmark in terms of shape quality and diversity. Moreover, after consistency distillation, our model is $100\times$ faster than the previous state-of-the-art in sampling.

II. RELATED WORKS

In this section, we discuss related works on diffusion models, accelerating diffusion models and 3D point cloud

generation, respectively.

A. Diffusion Models

Diffusion models reach state-of-the-art image synthesis by learning to invert a progressive noising process that corrupts data step by step. Under the standard discrete-time setup, the forward diffusion is a fixed Markov chain that progressively corrupts a clean sample into approximately Gaussian noise. The model is then trained to predict the injected noise or the score of the perturbed sample, enabling iterative denoising during sampling [26]. A complementary continuous-time perspective formulates diffusion as an SDE and learns the score of the perturbed data distribution. This view unifies diffusion and score-based generative modeling in a single framework and supports alternative sampling schemes [32, 33]. Maximum likelihood training for continuous-time score models further improves statistical efficiency and connects diffusion training to classic likelihood principles [34].

Scaling laws and architectural choices have made diffusion a robust default for high-fidelity image generation. Hierarchical or two-stage pipelines that combine powerful text encoders with diffusion backbones yield strong semantic control and photorealism [35, 36, 37]. Training the generative dynamics in a compact latent space rather than directly in pixel space substantially lowers compute and memory requirements while preserving visual fidelity, and has become a key enabler of high-resolution synthesis [24]. Compared with variational autoencoders and generative adversarial networks, diffusion models typically provide more stable optimization, reliable likelihood estimation, and improved mode coverage, mitigating common issues such as posterior collapse in VAEs and mode dropping in GANs [38, 39, 40]. During inference, samples are produced by integrating the learned reverse dynamics from noise toward data, which can be interpreted either as reversing a discrete diffusion chain or integrating an ODE or SDE defined by the learned score [26, 33].

B. Accelerating Diffusion Models

Despite their success, diffusion models are constrained by slow sampling due to many iterative denoising steps. Training-free acceleration exploits the continuous-time formulation to integrate probability-flow ODE trajectories in fewer steps, including high-order solvers such as DPM-Solver and its improved variants, as well as unified predictor-corrector samplers and adaptive step-size schemes [29, 41, 42]. Training-based acceleration modifies objectives or adds light retraining to shorten trajectories, where optimized discretization learns sampling times tailored to a fixed compute budget [43], truncated diffusion shortens the denoising horizon [44, 45], and neural-operator style learners amortize parts of the reverse dynamics [46]. Distillation compresses multi-step teachers into fast students by matching trajectories or terminal outputs, yielding few-step or even single-step generators [47, 48].

Recent works push one-step and few-step generation further. Consistency Models enforce a mapping that is consistent along time and can be trained either by distillation or from scratch, enabling rapid one-step sampling [30]. Follow-up

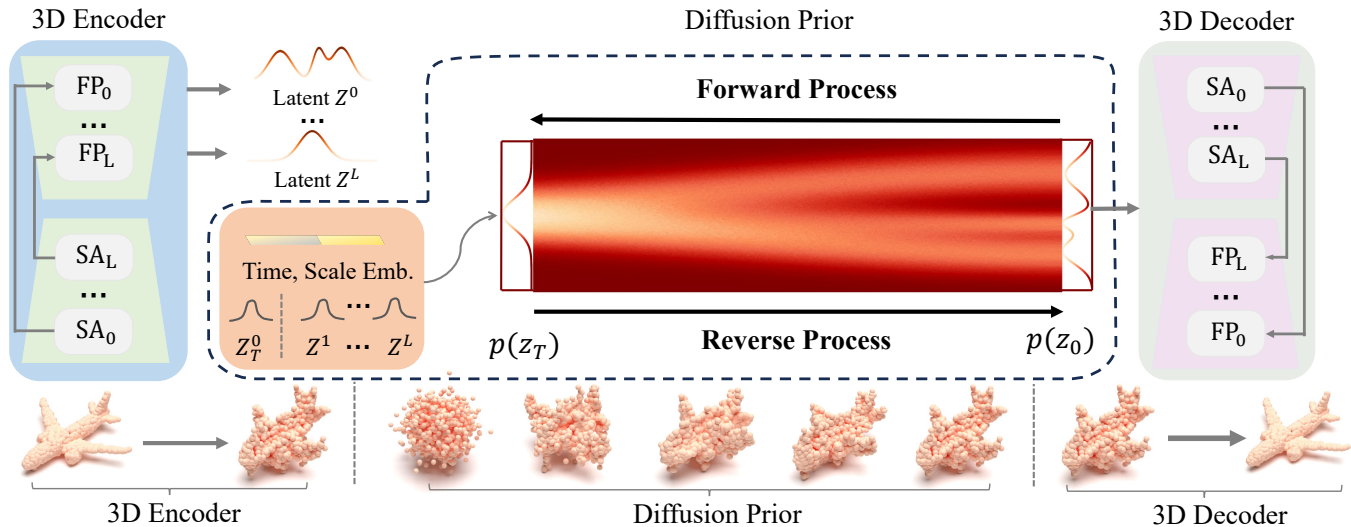


Fig. 1. An overview of the proposed multi-scale latent diffusion model. Hierarchical VAEs encode the input shape into latent variables at multiple resolutions, including point-level and super-point-level. Compared to the latent point diffusion model that only denoises the point-level latent space, our proposed multi-scale latent integration module injects higher-level latent variables to guide refinement, thereby jointly modeling local geometry and global structure. The details of the diffusion prior are shown in Figure 2.

advances improve training stability and data-only training, reduce reliance on perceptual losses, and formalize the theory of consistency training [49, 50]. Stochastic consistency distillation introduces noise-aware consistency to better align with the teacher’s trajectories and improve sample quality at low NFE [51]. In parallel, rectified-flow training has been strengthened to compete with distillation in the low-step regime, showing that a single reflow iteration with improved timestep curricula and robust pre-metrics is often sufficient [52]. Flow-matching and flow trajectory distillation style approaches provide another route to few-step or one-step sampling by directly parameterizing ODE paths from noise to data [53, 54]. There is also growing interest in faster training of diffusion and consistency models themselves, which leverages cross-init consistency phenomena and curriculum-style schedules to cut training cost while retaining generation quality [55]. Together, these strategies reduce latency by one to two orders of magnitude, making diffusion practical for interactive applications and deployment under strict compute budgets.

C. 3D Point Cloud Generation

This setting is commonly framed as 3D point shape and scene generation [12, 56, 57, 58]. Early work by Achlioptas *et al.* [59] formalized the problem with a simple GAN architecture built from stacked MLPs for both the generator and discriminator, and proposed quantitative criteria for assessing the realism of generated point sets. Subsequent studies strengthened the generative backbone by injecting structural inductive biases. Valsesia *et al.* [60] introduced graph-convolutional layers to better exploit neighborhood relations, while Liu *et al.* [61] adopted a tree-structured GCN to encode hierarchical dependencies among points. More recently, Gal *et al.* [62] explored a multi-root GAN formulation that can produce point clouds with emergent, unsupervised part-level factorization.

Not all point-cloud generators are GAN-based. A separate stream of work builds on explicit probabilistic formulations

[63, 64, 65]. ShapeGF [66], for instance, defines an (unnormalized) density over 3D space and then uses stochastic gradient ascent to nudge randomly seeded points toward high-density regions, which tend to concentrate around the target surface. Diffusion models offer a different interpretation [67, 68]. DPM [1] frames generation as running a particle-diffusion process in reverse. They start from noise and apply a shape-conditioned Markov denoising chain, motivated by analogies to thermal diffusion dynamics. There are also flow- and VAE-style approaches. PointFlow [12] casts a point set as a distribution of distributions and samples via continuous normalizing flows. ChartPointFlow [69] follows a similar path but introduces label-conditioned charts to better preserve topology. EditVAE [70], in turn, modifies the VAE framework to enable part-aware editing while still supporting unsupervised point-cloud generation.

Several lines of work suggest that plain auto-encoding setups are already quite competitive for learning point-cloud representations and reconstructing shapes such as I-GAN [59], ShapeGF [66], and the diffusion-based DPM [1]. Yet, even with steady progress in 3D generation, the deeper connection between GAN-based modeling and AE-style learning has received little systematic attention.

III. MULTI-SCALE LATENT POINT DIFFUSION MODELS AND LATENT CONSISTENCY MODELS

In this section, we will introduce our hierarchical VAE framework, the multi-scale latent point diffusion prior, and the latent consistency model.

A. Hierarchical VAE Framework

We begin by formally introducing the latent diffusion framework, which is essentially a hierarchical VAE. We denote a point cloud as $X \in \mathbb{R}^{N \times 3}$, consisting of N points with 3D coordinates. We then introduce a hierarchy of latent

variables with different spatial scales/resolutions, denoting as $\mathcal{Z} = \{Z^0, Z^1, \dots, Z^L\}$, where L is the number of hierarchy levels. We use superscript to denote the index of scales. Here $Z^l \in \mathbb{R}^{N_l \times C_l}$ where N_l and C_l are the number of points and the number of channels at the l -th level latent space respectively. Note that $C_l = 3 + D_l$, where D_l represents the extra dimension. At the 0-th, we have $N_0 = N$ and $N_l > N_{l+1}$ for any $l = 0, \dots, L-1$. In other words, the Z^0 is latent point representation whereas Z^l are latent super-point (*i.e.*, a subset of points) representations for any $l > 0$. The details of latent layers and points in each level are demonstrated in Section IV.

The backbone of our hierarchical VAE consists of an encoder $q_\phi(\mathcal{Z}|X)$, a decoder $p_\psi(X|\mathcal{Z})$, and a prior $p(\mathcal{Z})$, where ϕ and ψ are the learnable parameters. Specifically, our encoder is designed as follows,

$$q_\phi(\mathcal{Z}|X) := q_\phi(Z^L|X) \prod_{l=L-1}^0 q_\phi(Z^l|Z^{l+1}, X), \quad (1)$$

where $q_\phi(Z^l|X)$ and $q_\phi(Z^l|Z^{l+1}, X)$ are assumed to be factorized Gaussian distributions with learnable mean and fixed variance. Our decoder and prior take the simple form $p_\psi(X|\mathcal{Z}) := p_\psi(X|Z^0)$ and $p(\mathcal{Z}) := \prod_{l=0}^L p(Z^l)$ respectively. Here $p(Z^l) := \mathcal{N}(\mathbf{0}, I)$. We model the decoder $p_\psi(X|Z^0)$ as a fully factorized Laplace likelihood, where the location (mean) parameters are predicted by the network and the scale is fixed to 1. Under this choice, maximizing the reconstruction likelihood is equivalent to minimizing an L1 reconstruction loss.

The overall architecture is illustrated in Figure 1. As illustrated, both the encoder and decoder are built from stacked Set Abstraction (SA) and Feature Propagation (FP) modules. Each SA module contains point-voxel convolution (PVC) layers [71], followed by a Grouper block, which includes the sampling and grouping layers introduced by [17]. Each FP module consists of a nearest-neighbor interpolation operation, followed by MLPs and PVC layers.

First Stage Training. We optimize the encoder and decoder pair under a fixed prior by maximizing a modified evidence lower bound (ELBO),

$$\begin{aligned} \mathcal{L}_{\text{ELBO}}(\phi, \psi) = & \mathbb{E}_{p_{\text{data}}(X), q_\phi(\mathcal{Z}|X)} [\log p_\psi(X|\mathcal{Z}) \\ & - \lambda D_{KL}(q_\phi(\mathcal{Z}|X) \| p(\mathcal{Z}))]. \end{aligned} \quad (2)$$

Here $p_{\text{data}}(X)$ represents the unknown data distribution of 3D point clouds. The hyperparameter λ controls the trade-off between the reconstruction error and the Kullback-Leibler (KL) divergence.

B. Multi-Scale Latent Point Diffusion As Prior

After learning the encoder and the decoder in the first stage, we fix them and train a denoising diffusion based prior in the latent point space. Note that we have a set of latent representations $\mathcal{Z} = \{Z^0, \dots, Z^L\}$ ranging from point to super-point levels output by the hierarchical encoder. It is natural to select the latent variable with the coarsest scale (lowest spatial resolution), *i.e.*, Z^L , to build a diffusion prior since it would enable efficient diffusion in a low-dimensional latent space.

However, as demonstrated in prior work [2], point-level latent variables remain crucial for producing high-quality 3D shapes. We thus focus on the point-level latent variable Z^0 and design mechanisms to fuse multi-scale information. Specifically, we introduce a multi-scale latent point diffusion prior as below,

$$p(\mathcal{Z}) := p_\theta(Z^0|\mathcal{Z}^{\setminus 0}) \prod_{l=1}^L p_\theta(Z^l), \quad (3)$$

where $\mathcal{Z}^{\setminus 0} = \{Z^1, \dots, Z^L\}$. Here $p_\theta(Z^l)$ is again a factorized standard Normal distribution, whereas $p_\theta(Z^0|\mathcal{Z}^{\setminus 0})$ is a diffusion model. This design is crucial for enabling efficient sampling and consistency distillation, as it requires learning only one conditional prior while keeping others fixed. In contrast, previous work such as LION [2] needs to learn multiple priors corresponding to different levels in the hierarchy, which significantly complicates sampling and distillation. As in standard diffusion frameworks, our approach comprises a forward noising process and a learned reverse denoising process.

Forward Process. Following diffusion models [26], given initial latent point feature $Z^0 \sim q_\phi(Z^0|X)$ output by the encoder, we gradually add noise as follows,

$$q(Z_{1:T}^0|Z^0, \mathcal{Z}^{\setminus 0}) := \prod_{t=1}^T q(Z_t^0|Z_{t-1}^0), \quad (4)$$

$$q(Z_t^0|Z_{t-1}^0) := \mathcal{N}(Z_t^0; \sqrt{1 - \beta_t} Z_{t-1}^0, \beta_t I), \quad (5)$$

where $Z_0^0 := Z^0$ and we use subscripts to denote diffusion steps. T represents the number of diffusion steps, $q(Z_t^0|Z_{t-1}^0)$ is a Gaussian transition probability with variance schedule β_1, \dots, β_T . We adopt a linear variance schedule in the diffusion process. The choice of β_t ensures that the chain approximately converges to the stationary distribution, *i.e.*, standard Gaussian distribution $q(Z_T^0|Z^0, \mathcal{Z}^{\setminus 0}) \approx \mathcal{N}(Z_T^0; 0, I)$ after T steps.

Reverse Process. In the reverse process, given the initial noise $Z_T^0 \sim \mathcal{N}(Z_T^0; \mathbf{0}, I)$, we learn to gradually denoise to recover the observed latent point feature Z^0 as follows,

$$p_\theta(Z_{0:T}^0|\mathcal{Z}^{\setminus 0}) := p(Z_T^0) \prod_{t=1}^T p_\theta(Z_{t-1}^0|Z_t^0, \mathcal{Z}^{\setminus 0}), \quad (6)$$

$$p_\theta(Z_{t-1}^0|Z_t^0, \mathcal{Z}^{\setminus 0}) := \mathcal{N}(Z_{t-1}^0; \mu_\theta(Z_t^0, t, \mathcal{Z}^{\setminus 0}), \sigma_t^2 I), \quad (7)$$

where the mean function $\mu_\theta(\cdot, \cdot, \cdot)$ of the denoising distribution could be constructed by a neural network with learnable parameters θ . In particular, following DDPM, we adopt the reparameterization $\mu_\theta(Z_t^0, t, \mathcal{Z}^{\setminus 0}) = (Z_t^0 - \beta_t \epsilon_\theta(Z_t^0, t, \mathcal{Z}^{\setminus 0}) / \sqrt{1 - \bar{\alpha}_t}) / \sqrt{\alpha_t}$, where $\alpha_t := 1 - \beta_t$ and $\bar{\alpha}_t := \prod_{s=1}^t \alpha_s$. The variance σ_t is a hyperparameter and set to 1. Therefore, learning our multi-scale latent point diffusion prior is essentially learning the noise-prediction function $\epsilon_\theta(\cdot, \cdot, \cdot)$ parameterized by θ .

Second Stage Training. To train the prior, we ideally aim to minimize the KL divergence between the so-called *aggregated posterior* $q(\mathcal{Z}) = \int p_{\text{data}}(X) q_\phi(\mathcal{Z}|X) dX$ and the prior $p_\theta(\mathcal{Z})$. However, it is again intractable so that we need to resort to the negative ELBO, which can be equivalently written as the

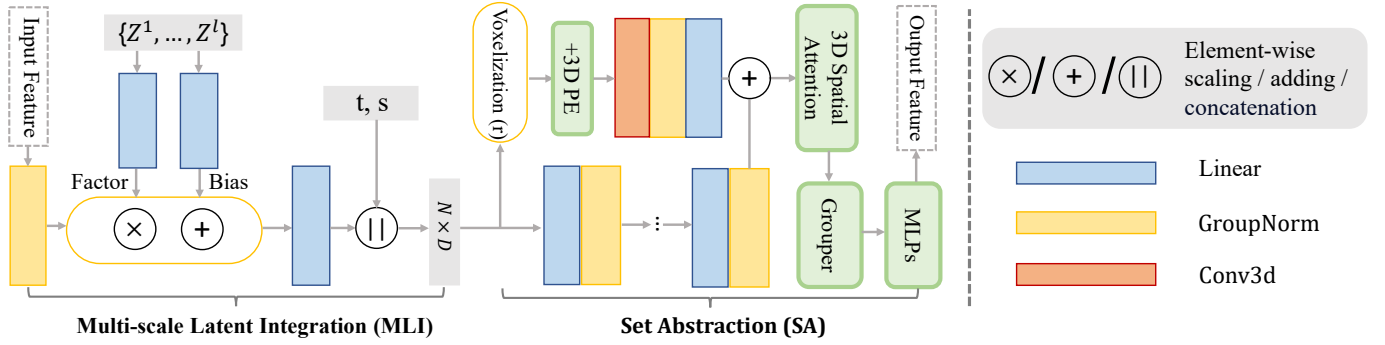


Fig. 2. An illustration of the network architecture of the latent diffusion prior. The multi-scale latent integration module injects higher-level latents to couple local geometry with global structure, while the set abstraction module downsamples and aggregates across scales. We denote the voxel grid size as r , and the hidden dimension as D .

following denoising score matching type of objective,

$$\mathcal{L}_{\text{SM}}(\theta) = \mathbb{E}_{t, X, \mathcal{Z}, \epsilon} \|\epsilon - \epsilon_{\theta}(Z_t^0, t, \mathcal{Z}^{\setminus 0})\|_2^2, \quad (8)$$

where the expectation is taken with respect to $t \sim U([T])$, $X \sim p_{\text{data}}(X)$, $\mathcal{Z} \sim q_{\phi}(\mathcal{Z}|X)$, $\epsilon \sim \mathcal{N}(\mathbf{0}, I)$. Here $U([T])$ represents the uniform distribution over $\{1, 2, \dots, T\}$. Following [2], we utilize the mixed score parameterization, which linearly combines the input noisy sample and the noise predicted by the network, resulting in a residual correction that links the input and output of the noise function ϵ_{θ} .

C. Architecture Design

We now introduce the specific architecture of our noise prediction function ϵ_{θ} . Our backbone network is based on Point-Voxel CNNs (PVCNNs) [71]. To integrate multi-scale latent point feature, we propose the multi-scale latent integration (MLI) module before each SA and FP module of PVCNNs. We also adopt a 3D spatial attention mechanism in each point-voxel convolution (PVC) module, allowing the model to selectively attend to informative areas, as shown in Figure 2.

Multi-Scale Latent Integration. To better capture geometric patterns of 3D shapes, we propose the multi-scale latent integration (MLI) module to fuse latent variables across multiple scales/resolutions. As shown in Figure 2, at the diffusion step t , the s -th MLI module takes the feature map F_s as input, where $F_0 = Z_t^0$. Specifically, given the high-resolution feature map F_s and the target feature F , we modulate the normalized target feature F with the scaling parameters of both the two-dimensional scale and the high-scale features F^i , resulting in an intermediate representation as follows:

$$F_{s+1} = \left[\text{MLP} \circ \text{ReLU}(\text{Linear}(Z^{\setminus 0}) \odot \text{Norm}(F_s) + \text{Linear}(Z^{\setminus 0}) \parallel \text{Pos}(t) \parallel \text{Pos}(k)) \right], \quad (9)$$

where Norm is the layer normalization [72] and Linear denotes a linear layer. MLP consists of two linear layers. \odot denotes element-wise product and \circ means function composition. $[\cdot \parallel \cdot]$ means concatenation of vectors. Pos(\cdot) is the positional embedding function. To enable scale-time awareness in the model, we further modulate the feature with positional em-

bedding of scale and time. The feature is fed to the following SA and FP modules to predict the noise.

3D Spatial Attention Mechanism. To help latent point representations better capture 3D spatial information, we design a 3D spatial attention mechanism. Our intuition is that closer points in 3D space would have a stronger correlation, thus higher attention values. We introduce a pairwise bias term that depends on the 3D distances between points. Specifically, in PVC, following [71], we first use PointNet++ [17] to extract the local features F_p from the point cloud. We then convert the point cloud data into voxels, enabling the application of 3D convolution operations to obtain voxel features F_v . These are then fused to get the combined feature $F_a = \text{Add}(F_p, \text{MLP}(F_v))$. For F_a , we compute the pairwise spatial distance matrix $B \in \mathbb{R}^{n^i \times n^i}$ between different point pairs at the current scale, where n^i is the number of points at the current scale i , and use it as a bias in computing the attention,

$$F_a = \text{softmax} \left(\frac{QK^T}{\sqrt{d}} + B \right) \cdot V, \quad (10)$$

where Q , K , and V are query, key, and value respectively in the standard attention module. We add this module to each PVC layer across all scales to make the model's attention conform to the 3D distances between points. Additionally, following [14], we add 3D positional embeddings to adaptively aggregate feature from voxelized point clouds. In each PVC layer, given voxelized input $V \in \mathbb{R}^{v \times v \times v \times c}$, where c is the embedding dimension and v^3 denotes the number of voxelized tokens, we add sine-cosine-based 3D positional embeddings to all input tokens.

D. Multi-Scale Latent Point Consistency Models

Since the diffusion models are notoriously slow in sampling, we explore the consistency models (CMs) [30] in the latent diffusion framework to accelerate the generation of 3D shapes. At the core of CMs, a consistency map is introduced to map any noisy data point on the trajectory of probability-flow ordinary differential equations (PF-ODEs) to the starting point, *i.e.*, clean data. There are two ways to train such a consistency map [30], *i.e.*, consistency distillation and consistency training. The former requires a pretrained teacher model whereas the latter trains the consistency map from scratch. We explored

both options and found consistency distillation works well, whereas consistency training is sensitive to hyperparameters.

Specifically, we first rewrite the reverse process in the continuous-time setting following [29, 33],

$$\frac{dZ_t^0}{dt} = \frac{d \log \alpha_t}{dt} Z_t^0 + \left(\frac{d \log \alpha_t}{2\sigma_t dt} - \frac{d \log \alpha_t}{dt} \sigma_t \right) \epsilon_\theta(Z_t^0, t, \mathcal{Z}^{\setminus 0}), \quad (11)$$

where $\epsilon_\theta(Z_t^0, t, \mathcal{Z}^{\setminus 0})$ is the noise prediction model and α_t, σ_t are determined by the noise schedule as aforementioned. Sampling corresponds to integrating the PF-ODE backward from T to 0. Following [30, 73], we instead learn a consistency mapping $f_{\hat{\theta}} : (Z_t^0, t, \mathcal{Z}^{\setminus 0}) \mapsto Z_0^0$ that directly outputs the PF-ODE endpoint Z_0^0 , enabling consistency distillation. At $t = 0$, we express $f_{\hat{\theta}}$ in terms of the noise predictor $\hat{\epsilon}_\theta$:

$$f_{\hat{\theta}}(Z_t^0, t, \mathcal{Z}^{\setminus 0}) = c_{\text{skip}}(t)Z_t^0 + c_{\text{out}}(t) \left(\frac{Z_t^0 - \sigma_t \hat{\epsilon}_\theta(Z_t^0, t, \mathcal{Z}^{\setminus 0})}{\alpha_t} \right), \quad (12)$$

where $c_{\text{skip}}(0) = 1$, $c_{\text{out}}(0) = 0$, and $\hat{\epsilon}_\theta(z, c, t)$ is a noise prediction model whose initialized parameters are the same as those of the teacher diffusion model. Note that $f_{\hat{\theta}}$ can be parameterized in various ways, depending on the teacher model’s parameterization of the diffusion model.

We assume a reliable ODE solver can approximate the integral in Eq. 11 over any time interval. The solver is used only during training, not at inference. We then learn to match the PF-ODE solution by minimizing a consistency distillation objective [30]:

$$\mathcal{L}_{\text{CD}}(\hat{\theta}, \hat{\theta}^-; \Psi) = \mathbb{E}_{n, \mathcal{Z}^{\setminus 0}, Z_{t_{n+1}}^0} \left[d \left(f_{\hat{\theta}} \left(Z_{t_{n+1}}^0, \mathcal{Z}^{\setminus 0}, t_{n+1} \right), f_{\hat{\theta}^-} \left(Z_{t_n}^0, \mathcal{Z}^{\setminus 0}, t_n \right) \right) \right], \quad (13)$$

where $\hat{Z}_{t_n}^0 = Z_{t_{n+1}}^0 + (t_n - t_{n+1})\Psi(Z_{t_{n+1}}^0, t_{n+1}, t_n, \mathcal{Z}^{\setminus 0})$ is the solution of the PF-ODE obtained via calling the ODE solver Ψ from time t_{n+1} to t_n . Here $d(\mathbf{x}, \mathbf{y}) = \|\mathbf{x} - \mathbf{y}\|_2^2$ denotes the discrepancy between two latent points, which penalizes large deviations more heavily and thus provides a smooth, scale-aware objective in the latent space.

IV. EXPERIMENTS

In this section, we train the multi-scale latent diffusion model on the Shapenet dataset and obtain MLPCM using the latent consistent distillation. We begin by describing the dataset and evaluation metrics, and then evaluate MLPCM on the single-class 3D point cloud generation benchmark. Next, we compare the results of MLPCM with a large number of baselines on multi-class unconditional 3D shape generation in terms of the performance, sampling time, and model parameters. Finally, we give a detailed ablation study on the effectiveness of individual contributions.

A. Datasets

For unconditional 3D point cloud generation, we adopt the ShapeNet benchmark [74] using the official PointFlow preprocessing pipeline [12] to keep the data protocol identical

to prior work. For a controlled and fair comparison against representative baselines [1, 2, 12, 14, 75], we restrict evaluation to the three standard categories most frequently reported in the literature: *airplane*, *chair*, and *car*.

Each ShapeNet instance is provided as a dense point set with 15,000 points. During optimization, we perform on-the-fly subsampling by uniformly drawing 2,048 points per shape at every iteration, which acts as lightweight data augmentation and matches the common experimental setup. The resulting training split contains 2,832 airplane shapes, 4,612 chair shapes, and 2,458 car shapes, ensuring that all methods are trained and evaluated under the same category scope and point budget.

During our re-implementation of several baselines on the PointFlow ShapeNet splits [12], we found that a subset of prior methods [2, 66, 76, 77, 78] adopts a *per-shape* normalization protocol rather than a global, dataset-level normalization. Concretely, for each individual shape, they compute axis-wise means to center the point cloud, and then estimate a shape-specific scale using the maximum spatial extent across the three axes. After this centering-and-scaling step, all coordinates are mapped to a bounded cube, typically within $[-1, 1]$.

To ensure apples-to-apples comparisons with these methods, we follow the same per-shape normalization procedure in both training and evaluation when reporting results against that group. This detail is non-trivial as different normalization strategies effectively define different learning problems. Global normalization preserves category-level variations in absolute scale and aspect ratios, whereas per-shape normalization removes such information and emphasizes normalized geometry only. As a result, the results across the two protocols are not directly comparable unless the normalization setup is explicitly aligned. We therefore report and interpret numbers only within the same normalization regime to maintain fairness and avoid misleading conclusions.

B. Implementation Details

Training Details We implement the teacher model in PyTorch [79] and optimize all components with Adam [80]. The VAE is trained for roughly 8,000 epochs, starting from a learning rate of 1×10^{-3} with a batch size of 128. We set the latent point dimensionality to 4 and use a skip weight of 0.01 to balance the reconstruction pathway during training. For the diffusion prior, we train for about 24,000 epochs with an initial learning rate of 2×10^{-4} . The diffusion process uses 1,000 time steps with a linear schedule. We then train MLPCM for 100K iterations, again with batch size 128, a learning rate of 2×10^{-4} , and an exponential moving average (EMA) decay of $\mu = 0.99995$ to stabilize optimization and improve sampling quality. Both the VAE and diffusion prior are trained on 8 NVIDIA A40 GPUs. Finally, our mixed denoising score network is implemented to exactly match the formulations in [2, 81].

Evaluation Metrics Consistent with prior studies [2, 12, 75], we evaluate using 1-NNA under both Chamfer Distance (CD) and Earth Mover’s Distance (EMD). This statistic compares the generated set against the validation distribution, jointly reflecting sample fidelity and diversity [12].

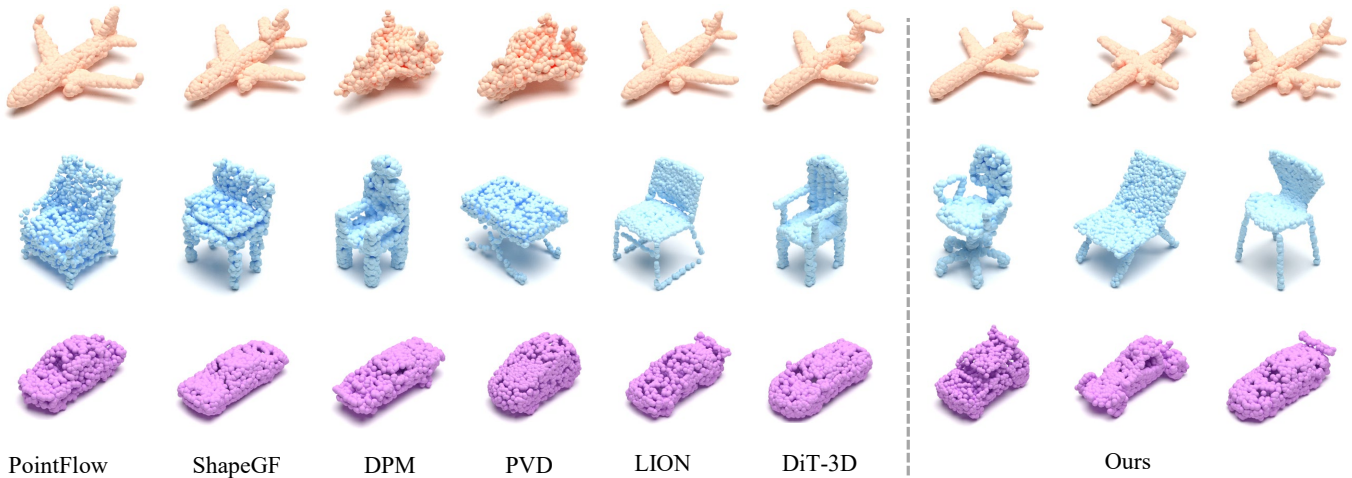


Fig. 3. We train class-specific ShapeNet models (*airplane*, *car*, *chair*) and generate 2,048-point unconditional samples with PointFlow-style global normalization. Our results better preserve part coherence such as seat-leg and wing-fuselage continuity, while prior methods often show disconnections, fused parts, or symmetry artifacts.

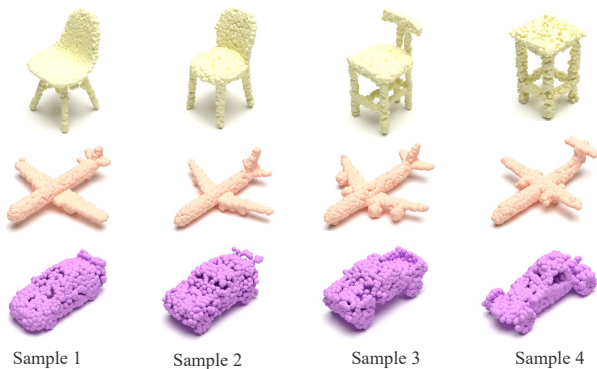


Fig. 4. Qualitative results show high-quality and diverse 3D assets. Samples maintain realistic structure and overall topology while exploring fine-grained detail changes, yielding diversity with symmetry largely intact.

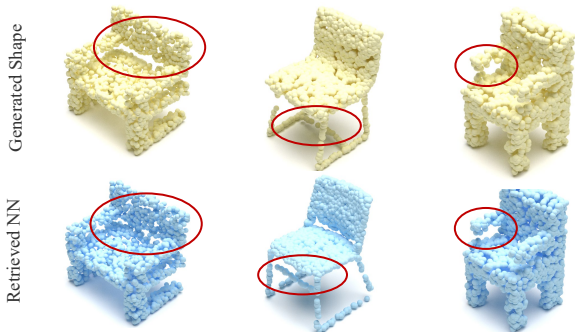


Fig. 5. Comparison between generated shapes and retrieved nearest neighbors (NN) in the training dataset. The generated shapes closely match the ground-truth shapes in overall topology, yet differ in fine-grained details, demonstrating diversity.

C. Single-Class 3D Point Cloud Generation

Implementation Our implementation is based on the PyTorch. The input point cloud size is 2048×3 . Both our VAE encoder and decoder are built upon PVCNN [71], consisting of 4 layers of SA modules and FP modules. The voxel grid sizes of PVC at different scales are 32, 16, 8, and 8, respectively.

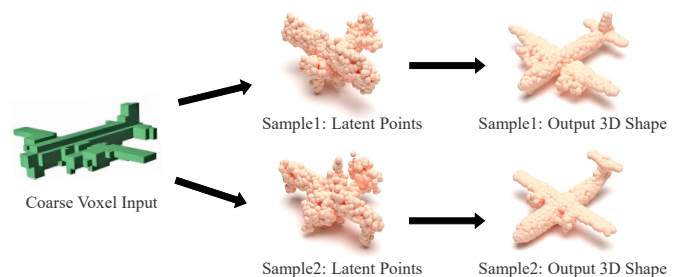


Fig. 6. Interactive voxel-guided generation. From a coarse occupancy grid, our model samples multiple plausible shapes that respect filled cells while sharpening geometry into smooth surfaces and well-formed parts.

We adopt the Farthest Point Sampling (FPS) algorithm for sampling in the Grouper block, with the sampled center points being 1024, 256, 64, and 16. KNN (K-Nearest Neighbors) is used to aggregate local neighborhood features, with 32 neighbors for each point in the Grouper. We apply a dropout rate of 0.1 to all dropout layers in the VAE.

Results We validate our model’s results under two settings: normalizing data across the entire dataset and normalizing each shape individually. Samples from MLPCM are shown in Figure 3 and Figure 4, and quantitative results are provided in Table I and Table II. For airplanes, our results better preserve thin structures and global symmetry, with crisper wing contours and fewer broken tips. Competing methods often exhibit wing thickening, tail erosion, or rough leading edges, especially in PointFlow and ShapeGF, while DiT-3D improves the silhouette but still shows uneven point density around the tail. For chairs, our method maintains slender legs with consistent spacing and recovers backrest curvature and armrest topology with clear connectivity, while other methods produce floating clusters near the seat or excessively smoothed armrests. Although LION and PVD capture the overall shape, they lose fine perforations and edge sharpness. For cars, our generations show clearly defined wheel arch depressions and fewer surface pits, whereas other methods yield blotchy

TABLE I

WE EVALUATE GENERATION ON THE *airplane*, *chair*, and *car* CATEGORIES OF THE POINTFLOW SHAPENET SPLIT [12] USING 1-NNA (LOWER IS BETTER). WE APPLY GLOBAL NORMALIZATION TO MAP THE TRAIN/TEST SETS INTO $[-1, 1]$. TM DENOTES THE TEACHER MODEL, AND LCM DENOTES LATENT CONSISTENCY MODELS.

Method	Airplane		Chair		Car	
	CD	EMD	CD	EMD	CD	EMD
r-GAN [59]	98.40	96.79	83.69	99.70	94.46	99.01
l-GAN (CD) [59]	87.30	93.95	68.58	83.84	66.49	88.78
l-GAN (EMD) [59]	89.49	76.91	71.90	64.65	71.16	66.19
PointFlow [12]	75.68	70.74	62.84	60.57	58.10	56.25
SoftFlow [82]	76.05	65.80	59.21	60.05	64.77	60.09
SetVAE [83]	76.54	67.65	58.84	60.57	59.94	59.94
DPF-Net [13]	75.18	65.55	62.00	58.53	62.35	54.48
DPM [1]	76.42	86.91	60.05	74.77	68.89	79.97
PVD [75]	73.82	64.81	56.26	53.32	54.55	53.83
LION [2]	67.41	61.23	53.70	52.34	53.41	51.14
MeshDiffusion [84]	66.44	76.26	53.69	57.63	81.43	87.84
DiT-3D [14]	69.42	65.08	55.59	54.91	53.87	53.02
Ours (TM)	65.12	58.70	51.48	50.06	51.17	48.92
Ours (LCM)	67.22	60.32	53.63	51.74	53.82	52.75

TABLE II

WE REPORT 1-NNA (LOWER IS BETTER) ON THE POINTFLOW SHAPENET BENCHMARK [12], USING PER-SHAPE NORMALIZATION TO MAP EACH EXAMPLE INTO $[-1, 1]$.

Method	Airplane		Chair		Car	
	CD	EMD	CD	EMD	CD	EMD
Tree-GAN [61]	97.53	99.88	88.37	96.37	89.77	94.89
ShapeGF [66]	81.23	80.86	58.01	61.25	61.79	57.24
SP-GAN [76]	94.69	93.95	72.58	83.69	87.36	85.94
PDGN [78]	94.94	91.73	71.83	79.00	89.35	87.22
GCA [77]	88.15	85.93	64.27	64.50	70.45	64.20
LION [2]	76.30	67.04	56.50	53.85	59.52	49.29
Ours (TM)	73.28	63.08	56.20	53.16	58.31	47.74
Ours (LCM)	75.56	66.85	58.58	55.32	61.28	49.91

TABLE III

RESULTS OF JOINT TRAIN ON 13 CLASSES OF SHAPENET-VOL.

Method	CD (1- NNA \downarrow)	EMD (1- NNA \downarrow)
Tree-GAN [61]	96.80	96.60
PointFlow [12]	63.25	66.05
ShapeGF [66]	55.65	59.00
SetVAE [83]	79.25	95.25
PDGN [78]	71.05	86.00
DPF-Net [13]	67.10	64.75
DPM [1]	62.30	86.50
PVD [75]	58.65	57.85
LION [2]	51.85	48.95
Ours (TM)	50.17	47.84
Ours (LCM)	53.85	52.45

bodies with collapsed cavities or roof perforations. DPM and ShapeGF in particular display pronounced surface granularity and local self-intersections.

More visual results generated by our multi-scale latent consistency model are demonstrated in Figure 7. Overall, our model achieves sharper thin structures, cleaner topology, and more uniform point distributions, leading to higher structural fidelity than other methods.

Note that TM stands for Teacher Model and LCM stands for Latent Consistency Models. MLPCM outperforms all baselines and achieves state-of-the-art performance across all categories and dataset versions. Compared to key baselines like DPM, PVD, and LION, our samples are diverse and have a better visual quality.

D. Multi-Class 3D Shape Generation

Following [2], We also perform joint training of the multi-scale latent diffusion model and MLPCM over 13 ShapeNet

categories, including airplane, chair, car, lamp, table, sofa, cabinet, bench, phone, watercraft, speaker, display, ship, and rifle. Due to the highly complex and multi-modal data distribution, jointly training a model is challenging.

We validated the model’s generation performance on the Shapenet-Vol dataset, where each shape is normalized, meaning the point coordinates are bounded within $[-1, 1]$. We report the quantitative results in Table III, comparing our method with various strong baselines under the same setting. We found that the proposed multi-scale latent diffusion model significantly outperforms all baselines, and MLPCM greatly improves sampling efficiency while maintaining performance.

E. Comparison with Nearest Neighbors and Voxel-guided Shape Synthesis

It is widely acknowledged that 1-NNA serves as the primary evaluation metric in this field, largely because no superior



Fig. 7. More visualization of Unconditional 3D shape generation via the proposed multi-scale latent consistency model on the airplane, car, and chair categories.

TABLE IV

THE SAMPLING RATES AND GENERATION QUALITY OF OUR MODEL WITH VARIOUS METHODS. OUR APPROACH ACHIEVES HIGH-QUALITY SHAPE GENERATION WITHIN 0.5 SECONDS WHILE MAINTAINING QUALITY.

Method	steps	time (sec)	CD (1- NNA↓)	EMD (1- NNA↓)
LION (DDPM) [2]	1000	27.09	53.41	51.14
LION (DDIM) [2]	1000	27.09	54.85	53.26
LION (DDIM) [2]	100	3.07	56.04	54.97
LION (DDIM) [2]	10	0.47	90.38	95.4
Ours (TM)	1000	25.16	51.17	48.92
Ours (LCM)	1	0.18	79.46	82.00
Ours (LCM)	4	0.31	53.82	52.75

TABLE V

ABLATION STUDIES ON KEY 3D DESIGN COMPONENTS ON THE CAR CATEGORY. PL AND SL REPRESENT THE POINT-LEVEL LATENTS AND SHAPE-LEVEL LATENTS, RESPECTIVELY, AND 3DSA REPRESENTS THE 3D SPATIAL ATTENTION MECHANISM.

PL	SL	3DSA	CD (1- NNA↓)	EMD (1- NNA↓)
	✓	✓	74.29	72.81
✓		✓	53.40	51.96
✓	✓		53.02	50.75
✓	✓	✓	51.17	48.92

TABLE VI

WE ABULATE THE ADDED LATENT-POINT FEATURE DIMENSION D_l ON THE CAR CATEGORY.

Extra Latent Dim	CD (1- NNA↓)	EMD (1- NNA↓)
0	54.56	52.79
1	51.17	48.92
3	56.88	55.27
5	59.06	51.90

TABLE VII

ABLATION RESULTS ON THE TEACHER MODEL ON THE CAR CATEGORY EVALUATE THE BACKBONE CHOICES IN THE HIERARCHICAL VAE AND THE DIFFUSION PRIOR. FOR DGCNN, WE ADDITIONALLY TEST DIFFERENT k VALUES IN THE k -NN GRAPH CONSTRUCTION.

Backbone	CD (1- NNA↓)	EMD (1- NNA↓)
DGCNN (knn=10)	67.66	57.08
DGCNN (knn=20)	68.54	57.60
PointTransformer	89.41	86.52
PointTransformerV2	80.09	79.57
PVCNN	51.17	48.92

TABLE VIII

ABLATION STUDY ON 3D POSITIONAL ENCODING ON THE CAR CATEGORY FOR TEACHER MODEL.

Settings	CD (1- NNA↓)	EMD (1- NNA↓)
w/o 3D PE	51.60	49.38
with VPE	51.17	48.92
with cRPE	51.10	49.08

alternative currently exists. However, it can be misleading, as perfect memorization of the training set would yield an excellent score. Therefore, we adopt a more informative analysis that present the generated shape alongside its retrieved nearest neighbor, highlighting their structural and semantic similarity while also illustrating diversity in finer details. Specifically, Fig. 5 compares our generated shapes (top) with their retrieved Chamfer-nearest neighbors (bottom). Global topology aligns closely, while fine details differ, confirming the diversity.

To supplement the conditional generation experiment to observe the generalization diversity of the model, We add voxel guided generation results as shown in Fig. 6. We begin by voxelizing the training set and fine-tuning our encoder networks to learn representations that can be accurately decoded back into the original shapes. For voxelized shapes handled by our point-cloud networks, we additionally extract surface samples from the voxel grids and use these points as the network inputs.

F. Sampling Time

The proposed multi-scale latent diffusion model synthesizes shapes using 1000 steps of DDPM, while MLPCM synthesizes them using only 1-4 steps, generating high-quality shapes in under 0.5 seconds. This makes real-time interactive applications feasible. In Table IV, we compare the sampling time and quality of generating a point cloud sample (2048 points) from noise using different DDPM, DDIM [28] sampling methods, and MLPCM. When using ≤ 10 steps, DDIM's performance degrades significantly, whereas MLPCM can produce visually high-quality shapes in just a few steps or even one step.

G. Ablation Study

In this section, we conduct an comprehensive ablation study to disentangle the effects of the main components in our multi-scale latent diffusion model. Specifically, we examine the impact of introducing multi-scale latent representations to capture both coarse global geometry and fine-grained local details, incorporating a 3D spatial attention mechanism to enable long-range dependency modeling and improved part-to-part coordination in 3D space, and augmenting the latent point representation with additional feature dimensions to increase expressiveness beyond pure coordinates. For each component, we report controlled comparisons under the same training protocol and evaluation metrics, and analyze how these choices affect generation fidelity, structural coherence, and sample diversity.

Ablation on the Key Design Components. We perform the ablation study on the Car category. For the configuration without multi-scale latent representations, we consider two scenarios: one using only point-level latent features to capture fine-grained details and another using only shape-level features to focus on global structure. This allows us to assess the impact of each representation scale individually. The model sizes are kept nearly identical across all settings to ensure fair comparison. As shown in Table V, the full model, integrating multi-scale latent representations and the 3D spatial attention mechanism, consistently outperforms the simplified settings across all evaluation metrics. This demonstrates the effectiveness of combining fine-grained local information with global shape context, along with the attention mechanism, in achieving more accurate and coherent reconstructions.

Ablation on Extra Dimension for Latent Points. We ablate the additional latent point dimension D_l on the Car category in Table VI. We experimented with several different additional dimensions for the latent points, ranging from 0 to 5, where $D_l = 1$ provided the best overall performance. As the additional dimensions increase, we observe a decrease in the 1-NNA score. We thus use $D_l = 1$ for all other experiments.

Ablation on different backbones. We conduct an ablation study to evaluate different neural network architectures for processing point clouds in the encoder, decoder, and diffusion prior. The results, presented in Table VII, focus on the car category using the teacher model, consistent with other ablation studies. We test four popular backbone architectures: Point-Voxel CNN (PVCNN) [71], Dynamic Graph CNN (DGCNN) [19], PointTransformer [56], and PointTransformerV2 [85]. Among these, PVCNN demonstrates the best overall performance, making it our architecture of choice.

Ablation on 3D Positional Encoding. We conduct an ablation study to evaluate different 3D positional encoding methods. In the Voxel Positional Encoding (VPE) approach, we applied frequency-based sine-cosine 3D positional embeddings to the point-voxel branch in the SA module, following the design of DiT-3D [14]. For Contextual Relative Positional Encoding (cRPE), inspired by the Stratified Transformer [86], we enhanced the traditional positional encoding in the attention mechanism by adding a vector representing the positional offset between Query and Key during each attention compu-

tation. The experiments were performed on the car category, with results summarized in Table VIII. The findings show that omitting 3D positional encoding leads to significantly poorer generation results. While VPE and cRPE achieve comparable outcomes, we selected VPE as our 3D positional encoding method for its simplicity and effectiveness.

V. CONCLUSION

In this paper, we propose the Multi-Scale Latent Point Consistency Model (MLPCM) to address the task of efficient point-cloud-based 3D shape generation. We first construct a multi-scale latent diffusion model, which includes a point encoder based on multi-scale voxel convolutions, a multi-scale denoising diffusion prior with 3D spatial attention, and a voxel-convolution-based decoder. The diffusion prior model, which integrates multi-scale information, effectively captures both local and global geometric features of 3D objects, while the 3D spatial attention mechanism helps the model better capture spatial information and feature correlations. Moreover, MLPCM leverages consistency distillation to compress the prior into a one-step generator. On the widely used ShapeNet and ShapeNet-Vol datasets, the proposed multi-scale latent diffusion model achieves state-of-the-art performance, and MLPCM achieves a $100\times$ speedup during sampling while surpassing the state-of-the-art diffusion models in terms of shape quality. In the future, we are interested in extending MLPCM to other 3D representations such as meshes.

REFERENCES

- [1] S. Luo and W. Hu, "Diffusion probabilistic models for 3d point cloud generation," in *Proceedings of the IEEE/CVF conference on computer vision and pattern recognition*, 2021, pp. 2837–2845.
- [2] X. Zeng, A. Vahdat, F. Williams, Z. Gojcic, O. Litany, S. Fidler, K. Kreis *et al.*, "Lion: Latent point diffusion models for 3d shape generation," *Advances in Neural Information Processing Systems*, vol. 35, pp. 10 021–10 039, 2022.
- [3] B. Du, X. Gao, W. Hu, and R. Liao, "Generative 3d part assembly via part-whole-hierarchy message passing," in *Proceedings of the IEEE/CVF Conference on Computer Vision and Pattern Recognition*, 2024, pp. 20 850–20 859.
- [4] M. Liu, R. Shi, L. Chen, Z. Zhang, C. Xu, X. Wei, H. Chen, C. Zeng, J. Gu, and H. Su, "One-2-3-45++: Fast single image to 3d objects with consistent multi-view generation and 3d diffusion," in *Proceedings of the IEEE/CVF conference on computer vision and pattern recognition*, 2024, pp. 10 072–10 083.
- [5] M. Chen, W. Yuan, Y. Wang, Z. Sheng, Y. He, Z. Dong, L. Bo, and Y. Guo, "Sketch2nerf: multi-view sketch-guided text-to-3d generation," *arXiv preprint arXiv:2401.14257*, 2024.
- [6] H. Wang, J. Cao, J. Liu, X. Zhou, H. Huang, and R. He, "Hallo3d: Multi-modal hallucination detection and mitigation for consistent 3d content generation," *Advances in Neural Information Processing Systems*, vol. 37, pp. 118 883–118 906, 2024.
- [7] Q. Tan, L. Gao, Y.-K. Lai, and S. Xia, "Variational autoencoders for deforming 3d mesh models," in *Proceedings of the IEEE conference on computer vision and pattern recognition*, 2018, pp. 5841–5850.
- [8] P. Mittal, Y.-C. Cheng, M. Singh, and S. Tulsiani, "Autosdf: Shape priors for 3d completion, reconstruction and generation," in *Proceedings of the IEEE/CVF Conference on Computer Vision and Pattern Recognition*, 2022, pp. 306–315.

- [9] J. Wu, C. Zhang, T. Xue, B. Freeman, and J. Tenenbaum, "Learning a probabilistic latent space of object shapes via 3d generative-adversarial modeling," *Advances in neural information processing systems*, vol. 29, 2016.
- [10] D. W. Shu, S. W. Park, and J. Kwon, "3d point cloud generative adversarial network based on tree structured graph convolutions," in *Proceedings of the IEEE/CVF international conference on computer vision*, 2019, pp. 3859–3868.
- [11] Z. Hao, A. Mallya, S. Belongie, and M.-Y. Liu, "Gancraft: Unsupervised 3d neural rendering of minecraft worlds," in *Proceedings of the IEEE/CVF International Conference on Computer Vision*, 2021, pp. 14 072–14 082.
- [12] G. Yang, X. Huang, Z. Hao, M.-Y. Liu, S. Belongie, and B. Hariharan, "Pointflow: 3d point cloud generation with continuous normalizing flows," in *Proceedings of the IEEE/CVF international conference on computer vision*, 2019, pp. 4541–4550.
- [13] R. Klokov, E. Boyer, and J. Verbeek, "Discrete point flow networks for efficient point cloud generation," in *European Conference on Computer Vision*. Springer, 2020, pp. 694–710.
- [14] S. Mo, E. Xie, R. Chu, L. Hong, M. Niessner, and Z. Li, "Dit-3d: Exploring plain diffusion transformers for 3d shape generation," *Advances in neural information processing systems*, vol. 36, pp. 67 960–67 971, 2023.
- [15] X. Ren, J. Huang, X. Zeng, K. Museth, S. Fidler, and F. Williams, "Xcube: Large-scale 3d generative modeling using sparse voxel hierarchies," in *Proceedings of the IEEE/CVF Conference on Computer Vision and Pattern Recognition*, 2024, pp. 4209–4219.
- [16] C. R. Qi, H. Su, K. Mo, and L. J. Guibas, "Pointnet: Deep learning on point sets for 3d classification and segmentation," in *Proceedings of the IEEE conference on computer vision and pattern recognition*, 2017, pp. 652–660.
- [17] C. R. Qi, L. Yi, H. Su, and L. J. Guibas, "Pointnet++: Deep hierarchical feature learning on point sets in a metric space," *Advances in neural information processing systems*, vol. 30, 2017.
- [18] J. Lei, J. Song, B. Peng, W. Li, Z. Pan, and Q. Huang, "C2fnet: A coarse-to-fine network for multi-view 3d point cloud generation," *IEEE Transactions on Image Processing*, vol. 31, pp. 6707–6718, 2022.
- [19] Y. Wang, Y. Sun, Z. Liu, S. E. Sarma, M. M. Bronstein, and J. M. Solomon, "Dynamic graph cnn for learning on point clouds," *ACM Transactions on Graphics (tog)*, vol. 38, no. 5, pp. 1–12, 2019.
- [20] W. Yuan, T. Khot, D. Held, C. Mertz, and M. Hebert, "Pcn: Point completion network," in *2018 international conference on 3D vision (3DV)*. IEEE, 2018, pp. 728–737.
- [21] L. P. Tchapmi, V. Kosaraju, H. Rezatofighi, I. Reid, and S. Savarese, "Topnet: Structural point cloud decoder," in *Proceedings of the IEEE/CVF conference on computer vision and pattern recognition*, 2019, pp. 383–392.
- [22] F. Fuchs, D. Worrall, V. Fischer, and M. Welling, "Se (3)-transformers: 3d roto-translation equivariant attention networks," *Advances in neural information processing systems*, vol. 33, pp. 1970–1981, 2020.
- [23] V. G. Satorras, E. Hoogeboom, and M. Welling, "E (n) equivariant graph neural networks," in *International conference on machine learning*. PMLR, 2021, pp. 9323–9332.
- [24] R. Rombach, A. Blattmann, D. Lorenz, P. Esser, and B. Ommer, "High-resolution image synthesis with latent diffusion models," in *Proceedings of the IEEE/CVF conference on computer vision and pattern recognition*, 2022, pp. 10 684–10 695.
- [25] A. Vahdat and J. Kautz, "Nvae: A deep hierarchical variational autoencoder," *Advances in neural information processing systems*, vol. 33, pp. 19 667–19 679, 2020.
- [26] J. Ho, A. Jain, and P. Abbeel, "Denoising diffusion probabilistic models," *Advances in neural information processing systems*, vol. 33, pp. 6840–6851, 2020.
- [27] J. Ho and T. Salimans, "Classifier-free diffusion guidance," *arXiv preprint arXiv:2207.12598*, 2022.
- [28] J. Song, C. Meng, and S. Ermon, "Denoising diffusion implicit models," *arXiv preprint arXiv:2010.02502*, 2020.
- [29] C. Lu, Y. Zhou, F. Bao, J. Chen, C. Li, and J. Zhu, "Dpm-solver: A fast ode solver for diffusion probabilistic model sampling in around 10 steps," *Advances in Neural Information Processing Systems*, vol. 35, pp. 5775–5787, 2022.
- [30] Y. Song, P. Dhariwal, M. Chen, and I. Sutskever, "Consistency models," *arXiv preprint arXiv:2303.01469*, 2023.
- [31] C. Lu, Y. Zhou, F. Bao, J. Chen, C. Li, and J. Zhu, "Dpm-solver++: Fast solver for guided sampling of diffusion probabilistic models," *arXiv preprint arXiv:2211.01095*, 2022.
- [32] Y. Song and S. Ermon, "Generative modeling by estimating gradients of the data distribution," *Advances in neural information processing systems*, vol. 32, 2019.
- [33] Y. Song, J. Sohl-Dickstein, D. P. Kingma, A. Kumar, S. Ermon, and B. Poole, "Score-based generative modeling through stochastic differential equations," *arXiv preprint arXiv:2011.13456*, 2020.
- [34] Y. Song, C. Durkan, I. Murray, and S. Ermon, "Maximum likelihood training of score-based diffusion models," *Advances in neural information processing systems*, vol. 34, pp. 1415–1428, 2021.
- [35] A. Ramesh, P. Dhariwal, A. Nichol, C. Chu, and M. Chen, "Hierarchical text-conditional image generation with clip latents," *arXiv preprint arXiv:2204.06125*, vol. 1, no. 2, p. 3, 2022.
- [36] A. Nichol, P. Dhariwal, A. Ramesh, P. Shyam, P. Mishkin, B. McGrew, I. Sutskever, and M. Chen, "Glide: Towards photo-realistic image generation and editing with text-guided diffusion models," *arXiv preprint arXiv:2112.10741*, 2021.
- [37] S. Shao, Z. Pei, W. Chen, D. Sun, P. C. Chen, and Z. Li, "Monodiffusion: Self-supervised monocular depth estimation using diffusion model," *IEEE Transactions on Circuits and Systems for Video Technology*, 2024.
- [38] D. P. Kingma, "Auto-encoding variational bayes," *arXiv preprint arXiv:1312.6114*, 2013.
- [39] K. Sohn, H. Lee, and X. Yan, "Learning structured output representation using deep conditional generative models," *Advances in neural information processing systems*, vol. 28, 2015.
- [40] I. Goodfellow, J. Pouget-Abadie, M. Mirza, B. Xu, D. Warde-Farley, S. Ozair, A. Courville, and Y. Bengio, "Generative adversarial networks," *Communications of the ACM*, vol. 63, no. 11, pp. 139–144, 2020.
- [41] C. Lu, Y. Zhou, F. Bao, J. Chen, C. Li, and J. Zhu, "Dpm-solver++: Fast solver for guided sampling of diffusion probabilistic models," *Machine Intelligence Research*, pp. 1–22, 2025.
- [42] W. Zhao, L. Bai, Y. Rao, J. Zhou, and J. Lu, "Unipc: A unified predictor-corrector framework for fast sampling of diffusion models," *Advances in Neural Information Processing Systems*, vol. 36, pp. 49 842–49 869, 2023.
- [43] D. Watson, J. Ho, M. Norouzi, and W. Chan, "Learning to efficiently sample from diffusion probabilistic models," *arXiv preprint arXiv:2106.03802*, 2021.
- [44] Z. Lyu, X. Xu, C. Yang, D. Lin, and B. Dai, "Accelerating diffusion models via early stop of the diffusion process," *arXiv preprint arXiv:2205.12524*, 2022.
- [45] H. Zheng, P. He, W. Chen, and M. Zhou, "Truncated diffusion probabilistic models," *arXiv preprint arXiv:2202.09671*, vol. 1, no. 3.1, p. 2, 2022.
- [46] H. Zheng, W. Nie, A. Vahdat, K. Azizzadenesheli, and A. Anandkumar, "Fast sampling of diffusion models via operator learning," in *International conference on machine learning*. PMLR, 2023, pp. 42 390–42 402.
- [47] T. Salimans and J. Ho, "Progressive distillation for fast sampling of diffusion models," *arXiv preprint arXiv:2202.00512*, 2022.
- [48] C. Meng, R. Rombach, R. Gao, D. Kingma, S. Ermon, J. Ho, and T. Salimans, "On distillation of guided diffusion models," in *Proceedings of the IEEE/CVF Conference on Computer Vision*

- and *Pattern Recognition*, 2023, pp. 14 297–14 306.
- [49] Y. Song and P. Dhariwal, “Improved techniques for training consistency models,” *arXiv preprint arXiv:2310.14189*, 2023.
- [50] Z. Geng, A. Pokle, W. Luo, J. Lin, and J. Z. Kolter, “Consistency models made easy,” *arXiv preprint arXiv:2406.14548*, 2024.
- [51] H. Liu, Q. Xie, T. Ye, Z. Deng, C. Chen, S. Tang, X. Fu, H. Lu, and Z.-J. Zha, “Scott: Accelerating diffusion models with stochastic consistency distillation,” in *Proceedings of the AAAI Conference on Artificial Intelligence*, vol. 39, no. 5, 2025, pp. 5451–5459.
- [52] S. Lee, Z. Lin, and G. Fanti, “Improving the training of rectified flows,” *Advances in neural information processing systems*, vol. 37, pp. 63 082–63 109, 2024.
- [53] X. Liu, C. Gong, and Q. Liu, “Flow straight and fast: Learning to generate and transfer data with rectified flow,” *arXiv preprint arXiv:2209.03003*, 2022.
- [54] X. Liu, X. Zhang, J. Ma, J. Peng *et al.*, “Instaflow: One step is enough for high-quality diffusion-based text-to-image generation,” in *The Twelfth International Conference on Learning Representations*, 2023.
- [55] T. Xu, P. Mi, R. Wang, and Y. Chen, “Towards faster training of diffusion models: An inspiration of a consistency phenomenon,” *arXiv preprint arXiv:2404.07946*, 2024.
- [56] H. Zhao, L. Jiang, J. Jia, P. H. Torr, and V. Koltun, “Point transformer,” in *Proceedings of the IEEE/CVF international conference on computer vision*, 2021, pp. 16 259–16 268.
- [57] Q. Hu and W. Hu, “Large scene generation with cube-absorb discrete diffusion,” in *Proceedings of the IEEE/CVF International Conference on Computer Vision*, 2025, pp. 25 186–25 196.
- [58] Q. Hu, Z. Zhang, and W. Hu, “Rangeldm: Fast realistic lidar point cloud generation,” in *European Conference on Computer Vision*. Springer, 2024, pp. 115–135.
- [59] P. Achlioptas, O. Diamanti, I. Mitliagkas, and L. Guibas, “Learning representations and generative models for 3d point clouds,” in *International conference on machine learning*. PMLR, 2018, pp. 40–49.
- [60] D. Valsesia, G. Fracastoro, and E. Magli, “Learning localized generative models for 3d point clouds via graph convolution,” in *International conference on learning representations*, 2018.
- [61] X. Liu, X. Kong, L. Liu, and K. Chiang, “Treegan: syntax-aware sequence generation with generative adversarial networks,” in *2018 IEEE International Conference on Data Mining (ICDM)*. IEEE, 2018, pp. 1140–1145.
- [62] R. Gal, A. Bermano, H. Zhang, and D. Cohen-Or, “Mrgan: Multi-rooted 3d shape representation learning with unsupervised part disentanglement,” in *Proceedings of the IEEE/CVF International Conference on Computer Vision*, 2021, pp. 2039–2048.
- [63] B. Zhang, M. Nießner, and P. Wonka, “3dilt: Irregular latent grids for 3d generative modeling,” *Advances in Neural Information Processing Systems*, vol. 35, pp. 21 871–21 885, 2022.
- [64] Y. Li, Y. Dou, X. Chen, B. Ni, Y. Sun, Y. Liu, and F. Wang, “Generalized deep 3d shape prior via part-discretized diffusion process,” in *Proceedings of the IEEE/CVF Conference on Computer Vision and Pattern Recognition*, 2023, pp. 16 784–16 794.
- [65] Y.-C. Cheng, H.-Y. Lee, S. Tulyakov, A. G. Schwing, and L.-Y. Gui, “Sdfusion: Multimodal 3d shape completion, reconstruction, and generation,” in *Proceedings of the IEEE/CVF Conference on Computer Vision and Pattern Recognition*, 2023, pp. 4456–4465.
- [66] R. Cai, G. Yang, H. Averbuch-Elor, Z. Hao, S. Belongie, N. Snavely, and B. Hariharan, “Learning gradient fields for shape generation,” in *Computer Vision—ECCV 2020: 16th European Conference, Glasgow, UK, August 23–28, 2020, Proceedings, Part III 16*. Springer, 2020, pp. 364–381.
- [67] Y. Zhou, D. Ye, H. Zhang, X. Xu, H. Sun, Y. Xu, X. Liu, and Y. Zhou, “Recurrent diffusion for 3d point cloud generation from a single image,” *IEEE Transactions on Image Processing*, vol. 34, pp. 1753–1765, 2025.
- [68] X. Cheng, L. Wu, Z. Wang, J. Hou, J. Wen, and Y. Xu, “Pvnet: Point-voxel interaction lidar scene upsampling via diffusion models,” *IEEE Transactions on Image Processing*, vol. 34, pp. 6895–6910, 2025.
- [69] T. Kimura, T. Matsubara, and K. Uehara, “Chartpointflow for topology-aware 3d point cloud generation,” in *Proceedings of the 29th ACM International Conference on Multimedia*, 2021, pp. 1396–1404.
- [70] S. Li, M. Liu, and C. Walder, “Editvae: Unsupervised parts-aware controllable 3d point cloud shape generation,” in *Proceedings of the AAAI Conference on Artificial Intelligence*, vol. 36, no. 2, 2022, pp. 1386–1394.
- [71] Z. Liu, H. Tang, Y. Lin, and S. Han, “Point-voxel cnn for efficient 3d deep learning,” *Advances in neural information processing systems*, vol. 32, 2019.
- [72] J. L. Ba, “Layer normalization,” *arXiv preprint arXiv:1607.06450*, 2016.
- [73] S. Luo, Y. Tan, L. Huang, J. Li, and H. Zhao, “Latent consistency models: Synthesizing high-resolution images with few-step inference,” *arXiv preprint arXiv:2310.04378*, 2023.
- [74] A. X. Chang, T. Funkhouser, L. Guibas, P. Hanrahan, Q. Huang, Z. Li, S. Savarese, M. Savva, S. Song, H. Su *et al.*, “Shapenet: An information-rich 3d model repository,” *arXiv preprint arXiv:1512.03012*, 2015.
- [75] L. Zhou, Y. Du, and J. Wu, “3d shape generation and completion through point-voxel diffusion,” in *Proceedings of the IEEE/CVF international conference on computer vision*, 2021, pp. 5826–5835.
- [76] R. Li, X. Li, K.-H. Hui, and C.-W. Fu, “Sp-gan: Sphere-guided 3d shape generation and manipulation,” *ACM Transactions on Graphics (TOG)*, vol. 40, no. 4, pp. 1–12, 2021.
- [77] D. Zhang, C. Choi, J. Kim, and Y. M. Kim, “Learning to generate 3d shapes with generative cellular automata,” *arXiv preprint arXiv:2103.04130*, 2021.
- [78] L. Hui, R. Xu, J. Xie, J. Qian, and J. Yang, “Progressive point cloud deconvolution generation network,” in *Computer Vision—ECCV 2020: 16th European Conference, Glasgow, UK, August 23–28, 2020, Proceedings, Part XV 16*. Springer, 2020, pp. 397–413.
- [79] A. Paszke, S. Gross, F. Massa, A. Lerer, J. Bradbury, G. Chanan, T. Killeen, Z. Lin, N. Gimelshein, L. Antiga *et al.*, “Pytorch: An imperative style, high-performance deep learning library,” *Advances in neural information processing systems*, vol. 32, 2019.
- [80] D. P. Kingma, “Adam: A method for stochastic optimization,” *arXiv preprint arXiv:1412.6980*, 2014.
- [81] A. Vahdat, K. Kreis, and J. Kautz, “Score-based generative modeling in latent space,” *Advances in neural information processing systems*, vol. 34, pp. 11 287–11 302, 2021.
- [82] H. Kim, H. Lee, W. H. Kang, J. Y. Lee, and N. S. Kim, “Softflow: Probabilistic framework for normalizing flow on manifolds,” *Advances in Neural Information Processing Systems*, vol. 33, pp. 16 388–16 397, 2020.
- [83] J. Kim, J. Yoo, J. Lee, and S. Hong, “Setvae: Learning hierarchical composition for generative modeling of set-structured data,” in *Proceedings of the IEEE/CVF Conference on Computer Vision and Pattern Recognition*, 2021, pp. 15 059–15 068.
- [84] Z. Liu, Y. Feng, M. J. Black, D. Nowrouzezahrai, L. Paull, and W. Liu, “Meshdiffusion: Score-based generative 3d mesh modeling,” *arXiv preprint arXiv:2303.08133*, 2023.
- [85] X. Wu, Y. Lao, L. Jiang, X. Liu, and H. Zhao, “Point transformer v2: Grouped vector attention and partition-based pooling,” *Advances in Neural Information Processing Systems*, vol. 35, pp. 33 330–33 342, 2022.
- [86] X. Lai, J. Liu, L. Jiang, L. Wang, H. Zhao, S. Liu, X. Qi, and J. Jia, “Stratified transformer for 3d point cloud segmentation,” in *Proceedings of the IEEE/CVF conference on computer vision and pattern recognition*, 2022, pp. 8500–8509.